Proceedings of the Institution of Mechanical Engineers, Part G: Journal of Aerospace Engineering,
Volume 233, Issue 13, 2019, pp. 4879-4894
DOI: 10.1177/0954410019831852

Original Article

Corresponding author:

Theoklis Nikolaidis, Cranfield University, Propulsion Engineering Centre, School of Aerospace, Transport, and Manufacturing, Bedfordshire, MK43 0AL, UK.

Email: t.nikolaidis@cranfield.ac.uk

CFD based approach for low-order models of propelling nozzle performance

Aws AL-Akam,

Cranfield University, Bedfordshire, UK

Theoklis Nikolaidis [1], David G. MacManus [1]

[1] Cranfield University, Bedfordshire, UK

Abstract

At the preliminary design stage for an aero-engine, the evaluation of the nozzle performance is an important aspect as it affects the overall engine cycle behaviour. Currently, there is a lack of systematic, extensive data on the nozzle performance and its dependence on the geometric and aerodynamic aspects. This paper presents a method that can be used to build characteristic maps for a nozzle as a function of a number of geometric and aerodynamic parameters. The proposed method encompasses the design of a nozzle configuration; a parameterisation of the nozzle pressure ratio (NPR), nozzle contraction ratio

Published by Sage. This is the Author Accepted Manuscript issued with: Creative Commons Attribution Non-Commercial License (CC:BY:NC 4.0).
The final published version (version of record) is available online at DOI:10.1177/0954410019831852. Please refer to any applicable publisher terms of use.

(CR), and plug-half angle (β); mesh generation, and an aerodynamic assessment using the Favre-Averaged Navier Stokes (FANS) method. The method has been validated against experimental performance data of a plug nozzle configuration and then used for the aerodynamic assessment.

The derived nozzle maps show that the thrust coefficient (C_{fg}) for this type of nozzle is significantly sensitive to the combined effect of the variation of the proposed parameters on the nozzle performance. These maps were used to build low-order models to predict C_{fg}, using response surface methods. The performance was assessed, and the results show that these low-order methods are capable of providing C_{fg} estimates with sufficient accuracy for use in preliminary design assessments.

Keywords: Propelling nozzle, nozzle aerodynamics, nozzle characteristics maps, thrust coefficient, Low order models

1. Introduction

The net thrust that is produced by the exhaust nozzle of an aero-engine is a function of the mass flow, velocity, static pressure at the nozzle exit and free stream static pressure [1]. The evaluation of the propelling nozzle performance is typically based on measuring how efficiently the nozzle produces the thrust with the least possible losses compared with the ideal thrust of the fully expanded nozzle [2]. The exhaust-system performance is typically assessed through the velocity (C_v), thrust (C_{fg}) and discharge (C_d) coefficients [3]. The velocity coefficient is the measure of the aerodynamic losses of the nozzle, excluding the external flow losses [3]. This gives a clear understanding of the way that the internal geometrical profile of the nozzle contributes to the nozzle performance. The thrust coefficient expresses the gross-thrust loss associated with imperfect nozzle expansion in addition to the internal losses [3]. The discharge coefficient (C_d) is the measure of the reduction in nozzle mass flow relative to the ideal

condition and is related to the required physical nozzle exit area to match the gas turbine thermodynamic cycle [4].

In addition to the operating conditions, the nozzle performance is affected by a number of geometrical aspects [3,5]. Thornock et al. [5] reported that the C_d is a function of the primary nozzle angle of the internal walls. Moreover, Zhang et al. [6], Spotts et al. [7] and Dippold et al. [8] showed that the half angle of the nozzle internal walls has an appreciable impact on the discharge and thrust coefficient. For a separate jet configuration, Lennard and Fasching [9] showed that the change in the curvature of the internal walls of the fan and core nozzles provided a 1.0% improvement in C_v at cruise conditions. Lahti et al. [10] assessed the impact of the inner aero-line curvature, in the region close to the nozzle throat, on the nozzle performance for a typical range of nozzle pressure ratio (NPR) from take-off to cruise conditions. The research showed that there is a noticeable influence of the throat inner wall curvature on the thrust coefficient. Two different nozzle geometries have been investigated by Malecki and Lord [11], with a different radius of curvature of the fan nozzle. The results showed that for the large radius of curvature of the hump nozzle efficiency increased by 1.0% at nozzle pressure ratio (NPR) of 1.6 and 2.1. Zimmermann et al. [12,13] investigated the effect of changing the length of the core-cowl for a separate jet configuration appropriate to an ultra-high by-pass ratio turbofan. The results showed that as the core-cowl length was increased, there was a reduction in the discharge coefficient of the fan nozzle and an increase in the thrust coefficient by 0.4% and 1.2%, respectively. On the other hand, the core nozzle showed an increase in the flow coefficient by 10% and a reduction in the thrust coefficient by 4.3%.

Overall, these previous studies showed that the nozzle design could have an important impact on the nozzle performance across a range of pressure ratios. However, although these studies highlight some of the aspects of nozzle

performance and sensitivities, there is a lack of systematic, extensive information on nozzle characteristics and how they depend on both geometric and aerodynamic aspects. The overall aim of this work is to identify typical key geometric and aerodynamic sensitivities and to propose an approach that could be used to develop nozzle characteristic maps for use in preliminary aero-engine design studies.

There has been extensive use of computational fluid dynamics (CFD) in the evaluation of a range of aero-engine nozzle characteristics. For example, Malecki and Lord [14] showed for a dual stream nozzle that the results from a Navier Stokes simulation using a standard k-ε turbulence model provided a thrust coefficient (C_{fg}) typically within 0.2% of the experimental data across the fan NPR of 1.6 to 2.41. Moreover, Zhang et al. [6] showed that results from a RANS simulation using the k-ω SST turbulence model were within 0.2% and 0.3% for C_d and C_{fg}, respectively, of the experimental data. This was for a three-dimensional single stream nozzle configuration across NPR range from 1.2 to 7.0. A CFD calculation using RANS and realizable k-ε turbulence model for the Dual Stream Flow Reference (DSFR) nozzle test case was performed by Mikkelsen et al. [15]. The results showed that the discharge coefficient (C_d) when compared with the measured data, had a difference of -0.35% at NPR of 2.60 and -0.67% at NPR of 1.40 for the fan nozzle, and a relative difference of +0.6% for the core nozzle. The overall thrust coefficient differed from the experimental data by 0.03%.

In summary, these previous studies showed that CFD simulations could provide evaluations of nozzle performance with sufficient accuracy that is, at least, pertinent to preliminary design studies. In the previous work, nozzle aerodynamic characteristics are still limited to a very few number of configurations. The available performance maps typically provide a single design parameter at the time. The present work uses the CFD model to establish nozzle performance maps as a function of the nozzle

pressure ratio (NPR), the plug half-angle (β) and the nozzle contraction ratio (CR). These performance maps were used to demonstrate that it is possible to build a low-order model to predict the nozzle characteristics which can be used in engine performance modelling or preliminary design.

2. Methodology

2.1 Nozzle geometry

A single-stream nozzle with a conical plug was chosen for the current work, (Figure 1). An analytical method based on Classification-Shape-Transformation (CST) was used for the parameterisation of the nozzle inner aero line and to ensure smooth surface definitions. The CST method was proposed first by Kulfan and Bussoletti [16], which was derived from the basic equations that govern the aerofoil geometrical-profile. This method was used to define the internal nozzle aero-lines (CDE and FG), (Figure 1). This method mainly produces a set of linear analytical functions that create smooth complex curves. The curves are connected by matching the spatial boundary conditions between the ends of each curve segment. Each segment has its unique system of linear equations depending on its spatial boundary conditions. The plug (GH) was designed using a circular arc and a straight line, (Figure 1). The afterbody of the cowl was designed using a simple circular-arc curve (AC), (Figure 1) with a slope angle of 13˚ relative the engine axis to avoid flow separation [17].

The initial nozzle exit area was calculated by a non-dimensional engine performance model based on a CF6-80E1 engine class [18]. The performance calculations were performed at mid-cruise operating conditions (Alt.=36,000ft, M_∞=0.82), and a thrust rating of 50.24kN. The total-temperature ratio of the nozzle inlet was kept constant at (T_t/T_∞=1.33) for all the range of NPR.

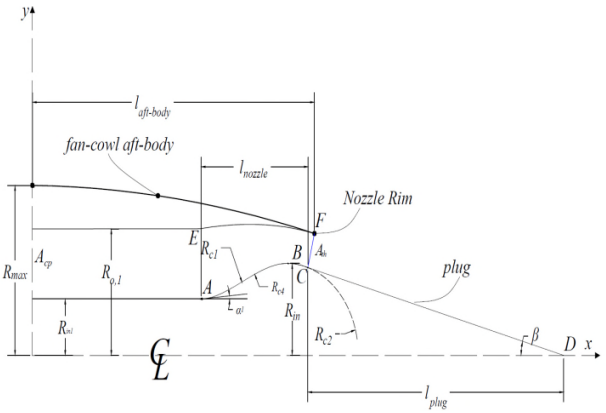


Figure 1 Section view of the nozzle configuration with the main geometrical lead parameters.

2.2 Nozzle parameterisation

The plug half-angle (β), nozzle contraction ratio ($CR=A_{cp}/A_{th}$) and nozzle pressure ratio (NPR) were changed. The CR was changed by modifying the nozzle throat area (A_{th}) by modifying the inner aero-line radius (R_{in}). Due to the complexity of the nozzle aero-line design, the change in any of the design parameters alters some additional geometrical constraints of the neighbouring components. To eliminate any mutual impact of a large number of design variables, some of the significant geometrical constraints were kept fixed. Therefore, when CR was changed β was kept constant, and the length of the plug was varied to meet the increase in the value of lower aero-line radius (R_{in}), (see Figure 1). The variation in the R_{in} changes the nozzle throat area and accordingly the CR. The CR was changed within the range from 1.30 to 1.74, (Table 1) with β from 10˚-20˚. For each configuration, the effect of NPR was evaluated across the range from 1.4 to 3.0. The NPR was varied by changing the inlet total-pressure of the nozzle. In total 17 simulations were performed to study NPR variation and 11 cases for β. These variations were applied to each nozzle CR to provide a total of 1122 simulations.

Table 1 Parameterisation cases of the nozzle

Case	$(CR = \frac{A_{cp}}{A_{th}})$	β (plug-half angle)	NPR [-]	M_{∞}[-]

1	1.30	10˚-20˚ (step 1.0˚)	1.4-3.0 (step 0.10)	0.82
2	1.40	10˚-20˚(step 1.0˚)	1.4-3.0(step 0.10)	0.82
3	1.53	10˚-20˚(step 1.0˚)	1.4-3.0(step 0.10)	0.82
4	1.60	10˚-20˚(step 1.0˚)	1.4-3.0(step 0.10)	0.82
5	1.67	10˚-20˚(step 1.0˚)	1.4-3.0(step 0.10)	0.82
6	1.74	10˚-20˚(step 1.0˚)	1.4-3.0(step 0.10)	0.82

2.3 CFD solutions

2.3.1 Domain sensitivity analysis and boundary conditions

The flow surrounding the nozzle was considered as being at 0.0° angle of attack, and therefore an axisymmetric domain was used for the simulations. The effect of the CFD domain size was assessed. The axial and the radial domain size were identified by $W=xD_{max}$ and $H= yD_{max}$, respectively, (Figure 2). The domain size was changed across a range of x from 30 to 120 and y from 10 to 30 with intervals of 30 and 10, respectively, (Figure 2). It was found that the variation between the domain size of x =90 and y=30 and x =120 and y =40 resulted in a thrust coefficient (C_{fg}) variation of $+6.0x10^{-5}$%. The third domain with $W = 90D_{max}$ and $H = 30D_{max}$ was chosen to carry out the simulations, (Figure 2).

The boundary conditions for the CFD model are the inlet pressure at the nozzle inlet, and the external domain inlet. A uniform profile of total pressure and temperature were applied to the inlet-pressure boundary conditions. The internal walls of the nozzle and the plug have been modified by the no-slip boundary conditions. Slip wall boundary condition was applied to the

domain boundaries extended from the location of the engine intake lip (of the full nacelle) to the inlet of the CFD domain (dashed line in Figure 2). The far-field boundary conditions were used to initialise the entire CFD domain.

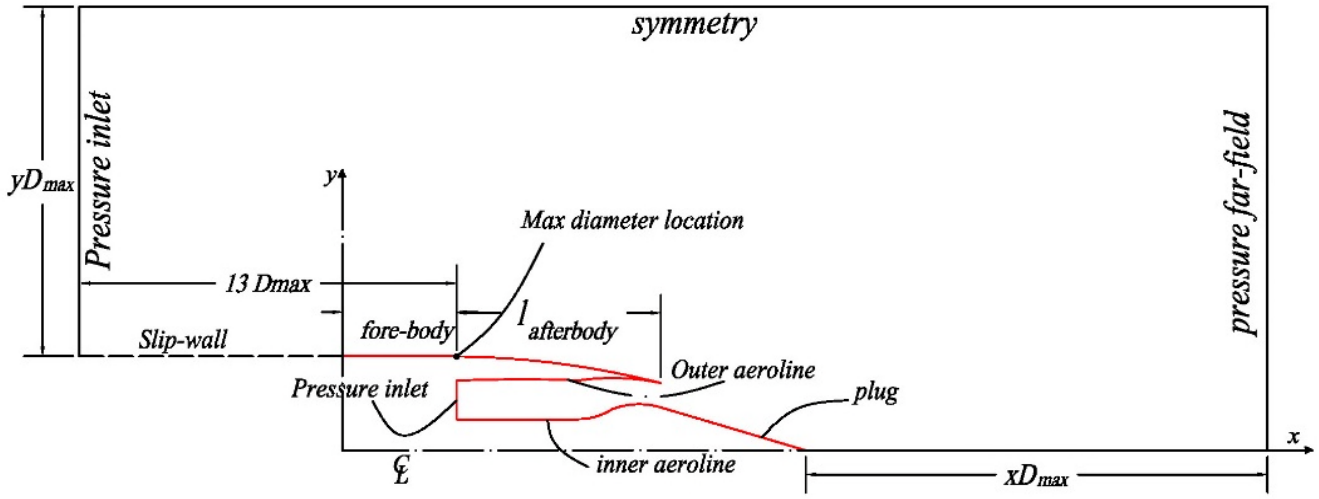


Figure 2 Boundary domain and boundary conditions of the nozzle CFD simulations.

2.3.2 Gridding method

A multi-block structured mesh topology was used to create the required mesh of the CFD domain. The mesh was refined sufficiently in a region where there are significant changes in the flow features, particularly in the exhaust jet region. The boundary layer was discretised to ensure the dimensionless wall distance (y^+) value close to one. The mesh-growth ratio in the radial direction was 1.20 for the boundary-layer region and 1.22 for the external domain.

A grid sensitivity study for the mesh was carried out, to ensure the credibility of the utilised mesh. Five meshes were generated to check the effect of the mesh size on the metrics of interest. The number of elements was increased from $8.6\text{x}10^4$ to $4.8\text{x}10^5$ with a refinement ratio of ≈1.45. The refinements were performed globally to ensure efficient distribution of the mesh across the CFD domain. The value of C_d and C_{fg} was assessed to check their dependence on the number of elements.

The last three meshes were chosen to report the Grid Convergence Index (GCI)[19] to assess the numerical behaviour of the meshes, Table 2. The $GCI_{1,2}$ was 0.03% for the computed $C_{fg,}$ and therefore the medium mesh with $3.25x10^5$ elements was chosen. The selection was based on considering the need to strike balance between the accuracy of the results and the time required to carry out the calculations.

Table 2 Grid sensitivity to the number of mesh elements based on the evaluation of GCI for the nozzle at operational conditions of M_∞=0.82 and NPR =2.5, for configuration of CR=1.75 and β =15˚.

f	(p)	$GCI_{1,2}$	$GCI_{2,3}$	$\frac{GCI_{1,2}}{r^p GCI_{2,3}}$
C_d	2.08	0.00727%	0.0188%	1.0
C_{fg}	2.23	0.0284%	0.06%	1.0

2.3.3 Numerical scheme

Favre-Averaged Navier-Stokes (FANS) numerical methodology coupled with the k-ω Shear-Stress Transport (SST) turbulence model was employed. A steady state, implicit and density-based solver was chosen to perform the simulations. The Green-Gauss node based method was used to compute the flow field gradients. A second-order accurate upwind scheme was employed for the spatial discretisation of the flow field. Sutherland's law was utilised for the calculations of dynamic viscosity [20].

A convergence strategy was conducted to achieve iterative convergence. The calculations were initialised using uniform free-stream flow conditions, and the CFL number was increased by two after every 500 iterations, up to CFL=20. After achieving converged residuals, the solver was switched to the second-order upwind scheme. The computations were continued until the residuals of the continuity equation reached the value of 10^{-5}, the momentum residuals achieved the value of $10^{-7,}$ and the turbulence equation residuals were of the order of 10^{-5}.

2.4 CFD model validation case

A validation task was performed to investigate the effectiveness of the FANS and the employed turbulence model in capturing the key features of the flow around the nozzle. For this purpose, a single-stream plug nozzle has been chosen as a validation test case for the employed CFD model. The aerodynamic parameters that were examined for in this exercise are M_∞ of 0.91 and NPR of 2.66 and 3.71 [21]. During the nozzle efficiency calculation, the NPR range was extended from 2.60 to 6.33 to be consistent with the experimental data. All the simulations were carried out at 0.0˚ angle of attack.

2.4.1 Geometry generation and boundary domain

The dimensions of the nozzle are presented in Table 3 [21]. The internal walls of the nozzle have been created using 5th order polynomial fitted curves to ensure smooth variation in the curvature of the wall inside the nozzle, Figure 3. The geometry was placed in a rectangular axisymmetric CFD domain. The details of the CFD domain and the boundary conditions are the same as used for the current nozzle model, (Figure 2). The distance from the nozzle rim to the CFD domain inlet was selected based on the boundary layer characteristics that are provided by Harrington [21], with momentum thickness to the maximum diameter ($\frac{\theta}{D_{max}}$) equals to 0.02. Harrington [21] found that the boundary layer velocity profile was similar to the 1/7th power law. Therefore, the length of the upstream distance from the nozzle rim was calculated based on the flat-plate turbulent boundary layer theory to achieve the provided boundary-layer thickness. The far-field boundary conditions were used to initialise the entire CFD domain.

Table 3 Lead dimensions of the validation plug nozzle.

D_{max} [cm]	l_{bt}/D_{max}	l_{pl}/D_{max}
55	1.30	1.80

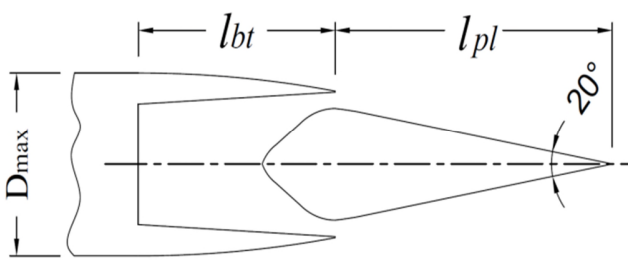


Figure 3 Sketch of the validation plug-nozzle configuration.

2.4.2 Mesh selection

Three meshes were generated to assess the effect of the number of cells on the properties of interest. The number of mesh elements was increased from $2.7x10^5$ to $7.6x10^5$ with an average refinement ratio of 1.66. The value of the drag coefficient of the boat-tail was assessed to check its dependence on the number of elements. The value of the $GCI_{1,2}$ (between the medium and fine mesh) is 0.026%. The medium mesh of $5.0x10^5$ was chosen to conduct the simulations. The numerical scheme and convergence criteria were the same as presented in basic nozzle configuration.

2.5 Nozzle performance calculation method

The nozzle performance is evaluated by estimating the non-dimensional metric of the gross thrust coefficient (C_{fg}). This is defined as the ratio of the gross thrust to the ideal gross thrust of the nozzle that is calculated at the design mass flow rate, (Equation (1)). The gross thrust of the engine is calculated by summation of the momentum flux and the pressure thrust of the nozzle. Exhaust-system components, such as the core-cowl or the plug could contribute to the engine thrust owing to the effect of the jet flow [12,22]. Therefore, It is vital to use an appropriate Thrust-Drag Bookkeeping (TDB) method for the assessment of the exhaust-system terms [2].

Two thrust coefficient definitions were utilised in the present work. One of the utilised definitions of the thrust coefficient includes the plug forces only in the calculation of gross thrust coefficient, ($C_{fg1,}$ Equation(2)) with $(F_G)_{pl}$ that is represented by Equation (3), and the other includes both the plug and the after-body forces (C_{fg2}, Equation (4)) with $(F_G)_{pl+aft\text{-}body}$ is calculated by Equation (5). These thrust

definitions were employed previously by Malecki and Lord [14] and Goulos et al. [22].

Where F_G represents the momentum flux and the pressure thrust at the charging plane of the nozzle. The ideal thrust is calculated based on Equation (6). The isentropic velocity (V_s) and the ideal mass flow rate and are calculated using Equation (7) and

(8) respectively[4,22]. Where $\left(NPR = \frac{P_t}{p_\infty}\right)$, R is the gas constant, γ is the heat capacity ratio and the, subscript (crit) denotes the choked NPR.

The pressure forces over the plug are represented by Φ_{pl}, Equation (9). The drag coefficient of the cowl after-body is represented by the $C_{Daft\text{-}body}$ term as defined in Equation (10). Where $D_{aft\text{-}body}$ is the drag force that is calculated by the integration of the pressure distribution over the cowl after-body surface and A_{ref} is the configuration reference area based on the nacelle max diameter. It should be mention that the force oriented downstream is the drag force and upstream is considered as thrust forces. The positive orientation in this work is considered downstream. For the validation task, the thrust was calculated using the thrust coefficient definition that included the plug and the aft-body forces, (C_{fg2}, Equation (4)) and it is consistent with that used in the experiment [21]. The ideal nozzle thrust (F_i) is calculated using the isentropic velocity and the actual mass flow rate ($F_i = \dot{m_a} V_s$).

$$C_{fg} = \frac{(F_G)}{Fi} \tag{1}$$

$$C_{fg1} = \frac{(F_G)_{pl}}{F_i} \tag{2}$$

$$(F_G)_{pl} = F_g - \left(\int_{pl} (p - p_\infty)d\vec{A} + \int_{pl} \tau\, d\vec{A}\right) \tag{3}$$

$$C_{fg2} = \frac{(F_G)_{pl+aft-body}}{F_i} \tag{4}$$

$$(F_G)_{pl+aft-body} = F_g - \left(\int_{pl+aft-body} (p - p_\infty)d\vec{A} + \int_{pl+aft-body} \tau\, d\vec{A}\right) \tag{5}$$

$$F_i = \dot{m_i} V_s \tag{6}$$

$$V_s = \sqrt{\frac{2\gamma RT_0}{(\gamma-1)}\left(1-\left(\frac{1}{NPR}\right)^{\frac{\gamma-1}{\gamma}}\right)} \quad (7)$$

$$(\dot{m})_i = P_0 A_i \left(\frac{1}{NPR_{crit}}\right)^{1/\gamma} \sqrt{\frac{2\gamma}{(\gamma-1)RT_0}\left(1-\left(\frac{1}{NPR_{crit}}\right)^{\frac{\gamma-1}{\gamma}}\right)} \quad (8)$$

$$\Phi_{pl} = \int_{pl} (p - p_\infty) d\vec{A} \quad (9)$$

$$C_{Daft-body} = \frac{D_{aft-body}}{0.5\,\rho U_\infty^2 A_{ref}} \quad (10)$$

2.6 Response surface methods

Response surface methods (RSM) are data-based techniques. They perform well when there is a large number of accurate data provided. RSM offers techniques to capture the impact of the responses as a function of varying levels of control factors that are identified to govern physical processes. RSM is dependent on the use of regression analysis on data from experiments or computational fluid dynamic (CFD) simulations at multiple levels.

The strength of the RSM techniques lies in capturing efficient and smooth approximations for accurate data generated from numerical or practical experiments at discretised data points in the design space [23]. The selection of the equations to represent the behaviour of any set of data has a great influence on the accuracy of the newly predicted response.

This work examines the accuracy, and the ability of the three different Response Surface Method (RSM) approaches to predict the nozzle performance metrics based on the CFD computed data. The selected RSM models are linear [24], Cubic Spline (CS) [25] and Kriging [26] methods. The RSMs were applied on a two-dimensional design space based on the nozzle pressure ratio (NPR) and the plug half angle (β). The overall aim is to demonstrate the ability of selected RSM approaches to map multidimensional patterns of the performance metric of the exhaust-system as a function of different levels of aerodynamic and geometric parameters that are identified to affect the overall aero-engine performance.

To ensure the credibility of the employed models in evaluating the performance metrics, a validation of the predicted RSM results was performed using a Cross-Validation (CV) approach [27]. The Leave-One-Out approach (LOO) was employed, to estimate the test error associated with using a specific RSM on a set of observations based on the nozzle C_{fg}. This approach is performed by removing one data point (test data) out of the entire observed data (nozzle performance data) and rebuilding the prediction model on the rest of the set of the data to provide a prediction for the removed test data point. The absolute difference between the predicted and the computed performance metrics (ΔC_{fg}) is then calculated.

The linear RSM technique is based on connecting any two neighbouring data points by a straight line [28]. The interpolated data point is guaranteed to be bounded by the value of the surrounding data points. In another word, the main influencer on the response is the closest data point values only. For the current work, the linear interpolation was used as RSM to predict the nozzle performance metrics as a function of the NPR and β.

To increase the smoothness of the curve that is connecting a pair of data point a polynomial with a third order cubic spline can be used [25]. This third-order polynomial was derived for each interval between two data points. Therefore, for n+1 data points, there are four times n unknown conditions need to be evaluated. Same design variables that have been changed in the linear RSM were utilised here.

One of the well known RSM methods is Kriging. It is an interpolation approach which uses least-square estimation to minimise the discrepancy between the predicted and the original data[29]. Kriging methods use spatial correlations between the original data points based on Gaussian exponential function [26]. Simple Kriging was employed in the current analysis using an absolute exponential correlation. The regression function was considered to be quadratic and the nugget value of 1.0×10^{-11}. The upper and the lower theta was chosen to be 0.1 and 0.0001, respectively.

3. Results and Discussion

3.1 Validation case results

3.1.1 Nozzle aerodynamics

The local static pressure distribution over the plug surface (P_{pl}) was normalised by the nozzle inlet total pressure at the charging plane (P_{cp}), to be consistent with the experimental data. The CFD results show that, at transonic Mach number (M_∞=0.91) and *NPR* of 2.66, the static pressure ratio distribution ($\frac{p_{pl}}{P_{cp}}$) over the plug surface agrees with the experimental data, (Figure 4). The absolute difference of the average pressure ratio $\Delta(\frac{p_{pl}}{P_{cp}})_{ave}$ is 0.127% along the plug length. At higher NPR (3.71), the numerical model generally predicts the location and strength of the expansion and compression waves over the plug. The only exception is at one data point located at $x/l_{pl} \approx 0.5$, (Figure 4). It can be concluded that the CFD approach is able to capture the key features of the flow that affect the nozzle performance.

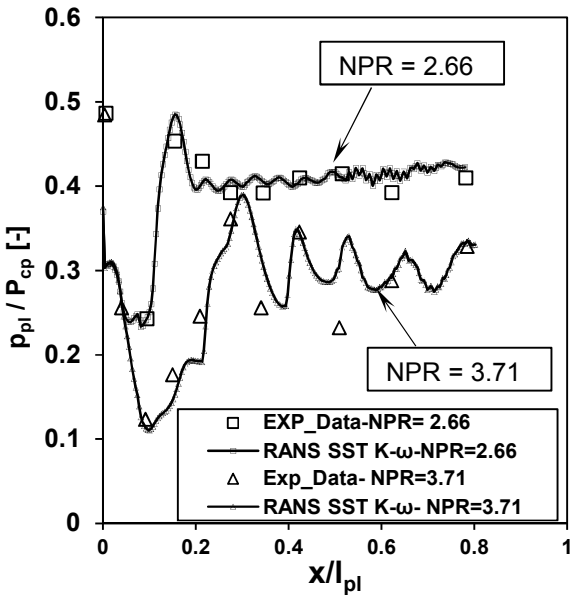


Figure 4 Comparison of plug surface pressure distribution between the CFD models and the experimental data at free stream M∞ of 0.91 and two NPR 2.66 and 3.71.

3.1.2 Nozzle efficiency

The calculated results that are obtained using the modified thrust coefficient definition (C_{fg2}) generally agreed well with the experimental data, (Figure 5). For example, there was a difference between the CFD results and the measurements of nozzle efficiency (C_{fg2}) of -1.05% at NPR =2.64 and from -0.46% to -0.68% between NPR =3.14 to 5.3. Previous work by Malecki and Lord [14], reported slightly

larger differences of -0.70% to -0.84%. Overall the current method is considered sufficiently useful to explore the nozzle design space.

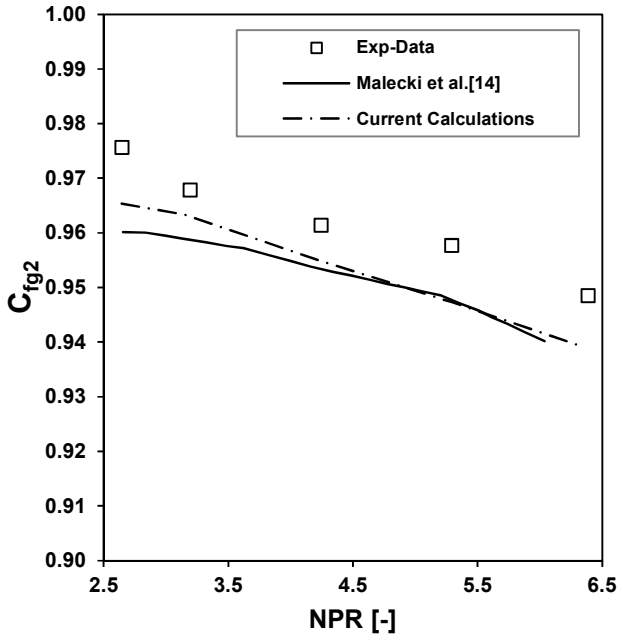


Figure 5 Comparison between the CFD and the experimental plug nozzle efficiency at M_∞ = 0.91 and the chosen NPR**.**

3.2 Nozzle aerodynamic results

The results are presented in a sequence that provides a detailed discussion of the influence of the investigated parameters followed by a presentation of the nozzle maps.

3.2.1 The impact of nozzle pressure ratio (NPR)

The NPR ranged from 1.4 to 3.0 to cover the range of the unchoked and choked nozzle conditions and thereby simulating different flight operating conditions for the nozzle. The NPR was increased by changing the inlet total pressure of the nozzle; in ideal cases as the NPR increase to levels greater than the critical NPR the nozzle is considered to be choked. At this stage, the further increase in the NPR will not affect the mass flow rate, and the external pressure fluctuation will not affect the internal flow properties of the nozzle. However, increasing the NPR of the nozzle increases the static pressure distribution around the exit. This can be seen when the NPR increased to 3.0 the pressure coefficient (C_p) is 1.9, (Figure 6). This indicates an under-expanded behaviour of the nozzle flow which results in a shock structure across a range of the NPR from 2.4 to 3.0, (Figure 7). The strength and the distance between the compression pressure waves

increase with the NPR, (Figure 7). The presence of the shock structure increases the pressure forces over the plug, and since the cone surface is inclined backwards, the pressure force contributes positively to the gross thrust of the nozzle. On the other hand, due to the expansion of the flow in the nozzle jet, there are some regions where the pressure is negative over the plug. These regions are expressed by is a low-pressure area, that appears at high NPR (2.6-3.0) (Figure 6). These negative pressure regions could contribute as a drag force. However, the effect of these regions is relatively small in comparison with the size and magnitude of the positive pressure regions. Even though there is an increase in the pressure forces of the plug with NPR the ratio (Φ_{pl}/F_i) showed a declining trend (Figure 8).

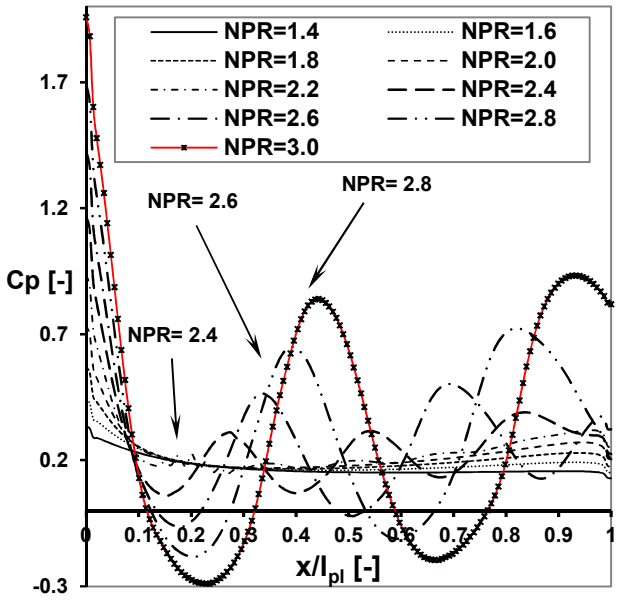
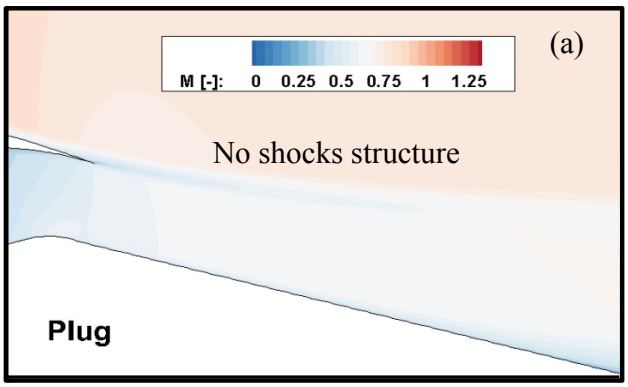


Figure 6 Pressure coefficient (Cp) distribution over the plug surface at different NPR, for the configuration of CR=1.4, and $\beta = 10^{\circ}$.



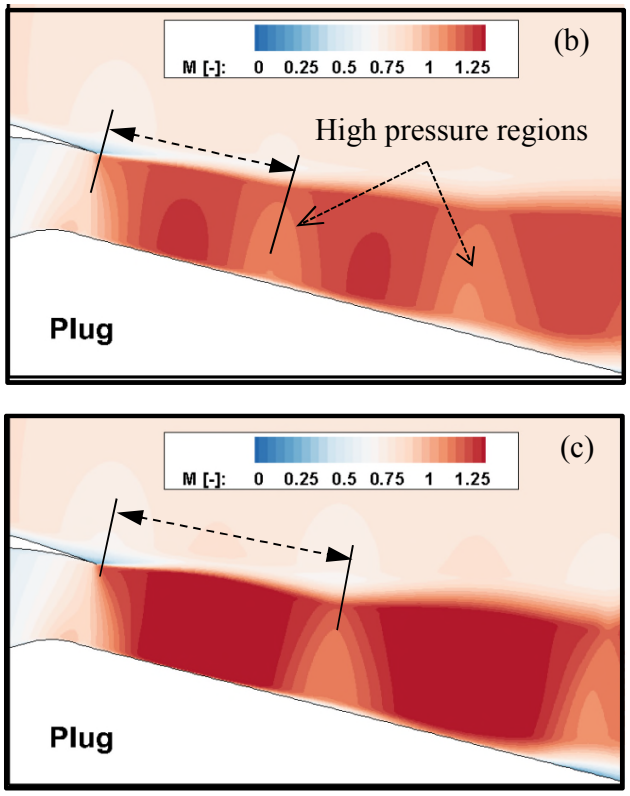


Figure 7 Mach number distribution for the flow around the nozzle for the configuration of CR=1.4, and β =10˚ at different NPR; (a) NPR = 1.4, (b) NPR =2.6, NPR =3.0.

The increase in the NPR also affects the pressure distribution over the cowl aft-body surface. This behaviour results in a reduction in the relative drag pressure forces of the cowl aft-body ($\frac{\Phi_{cowl\ aft-body}}{F_i}$) as NPR is increased (Figure 8). This reduction in $\frac{\Phi_{cowl\ aft-body}}{F_i}$ was produced due to the reduction in the inclination angle of the exhausted jet from the nozzle.

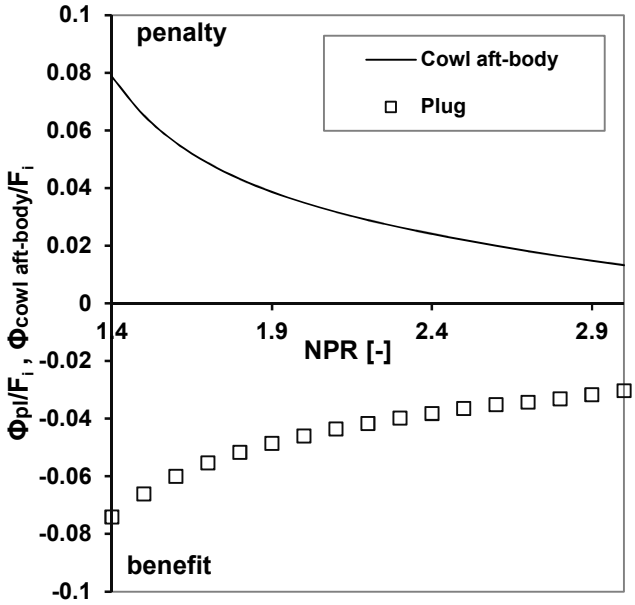


Figure 8 Pressure forces over the cowl after-body (Φ_{cowl}) and the plug (Φ_{pl}) normalised (F_i) to the ideal thrust as a function of the NPR, for the configuration of CR=1.40, and β =10˚.

3.2.2 Impact of the plug half-angle (β)

The increase in the plug half-angle (β) affects the pressure distribution over the cone surface due to the variation in the post-exit stream tube angle, (Figure 9). Moreover, strong shock waves were noticed over the cone surface with the increase in β from 10˚ to 20˚, (Figure 10). The

presence of these shocks intensified the pressure levels over the plug surface, as presented in Figure 9. The pressure coefficient (Cp) increased ΔCp by about 0.02 at the plug edge (x/l=0.98, point H in Figure 1), when β was increased from 10˚ to 20˚ at low NPR (1.4), with ΔCp of ≈0.022 for every step of 2˚ in β, (Figure 9).

The increase in the plug surface pressure, as a result of the increase in β, causes an increase in the pressure forces(Φ_{pl}/F_i), (Figure 11). The increase in the plug pressure forces (Φ_{pl}/F_i) with NPR is noticeable at low NPR, in which the plug force difference between the two extreme angles (β=10˚ and 20˚) is ≈0.040 at NPR =1.4. However, this difference reduces owing to the increase in the NPR, to 0.013 at NPR =3.0. The variation of the pressure force becomes insignificant between β =19˚ and β =20˚ across the range of NPR from 2.8 to 3.0. This can be attributed to little variation in the jet angle with the further increase in β. At high β levels, the jet is not attached to the plug surface because of the presence of strong shock close to the nozzle exit.

The impact of changes in β on the cowl after-body drag coefficient $C_{Daft\text{-}body}$ is significant, (Figure 12). The change in the plug angle means a variation in the stream-tube shape. Increasing the angle of the plug moves the post-exit stream-tube radially inwards and, consequently, the area of the external stream-tube over the jet increases. This increase reduces the pressure over the cowl after body. Consequently, there is an increase in the aft body drag coefficient ($C_{Daft\text{-}body}$) (Figure 12). This behaviour was noted across a range of from 10 to 14. However, across the range of the NPR between 1.4 and 2.0 and β between 15˚ to 20˚, the drag coefficient ($C_{Daft\text{-}body}$) increased, (Figure 12). This behaviour is dissimilar to the results of β value through the range from 10˚ to 14˚. This increase in the drag forces in this region can be attributed to the increase in the size of the stream-tube towards the plug surface at the beginning of the formation of the exhaust jet. Therefore, the external free stream is directed towards the

engine axis, across this range of NPR. This behaviour shows the importance of having a multi-degree of freedom aerodynamic analysis for the nozzle. Because doing only single parameter analysis could not provide the full characteristics of the aerodynamic behaviour of the nozzle.

In the end, the variation in the value of the plug half angle has a dual impact on the nozzle aerodynamics. The first impact is on the pressure forces over the plug surface and the second on the cowl afterbody pressure. These impacts on the pressure forces can be attributed to the variation in the pressure levels that are surrounding the nozzle. Since the NPR variation affects the pressure field as well, there will be an interaction between both influences. Therefore, the impact of β and NPR has to be considered collectively.

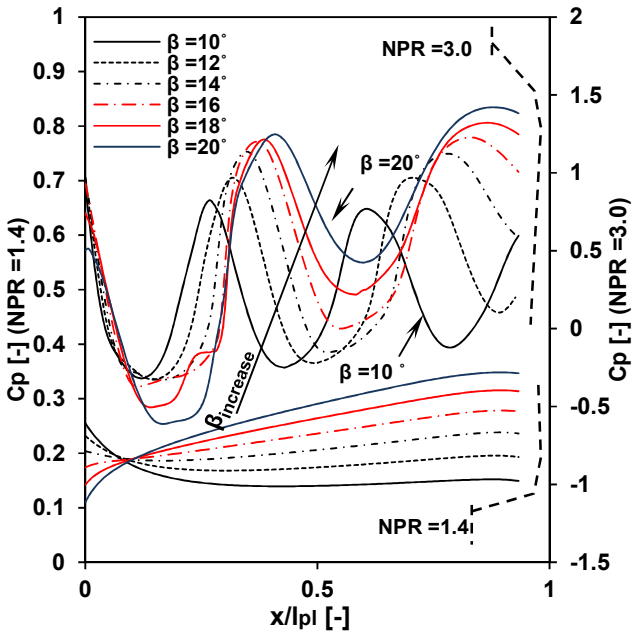
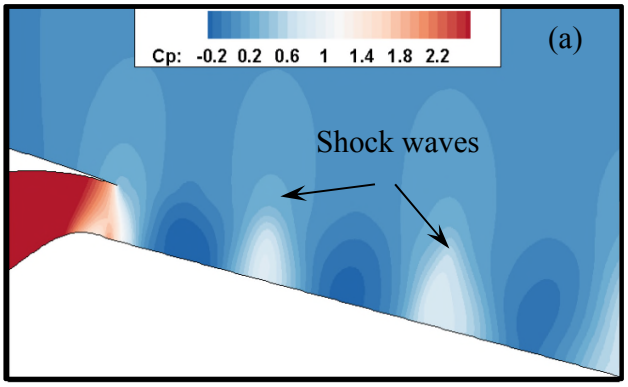


Figure 9 Pressure coefficient (Cp) distribution over the plug surface at NPR =1.4 and 3.0, at the chosen plug half angle (β), at operational conditions of M_∞ =0.82 and Alt =36000 ft, for the configuration of CR=1.75.



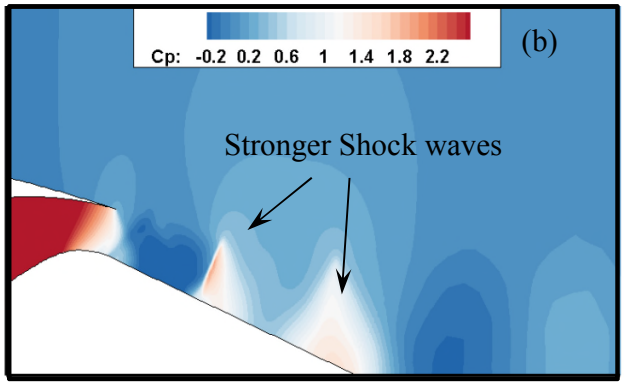


Figure 10 pressure coefficient (Cp) distribution around the plug for nozzle configuration of CR= 1.75 and for NPR =3.0 for two β levels; (a) β =10˚, (b) β =20˚.

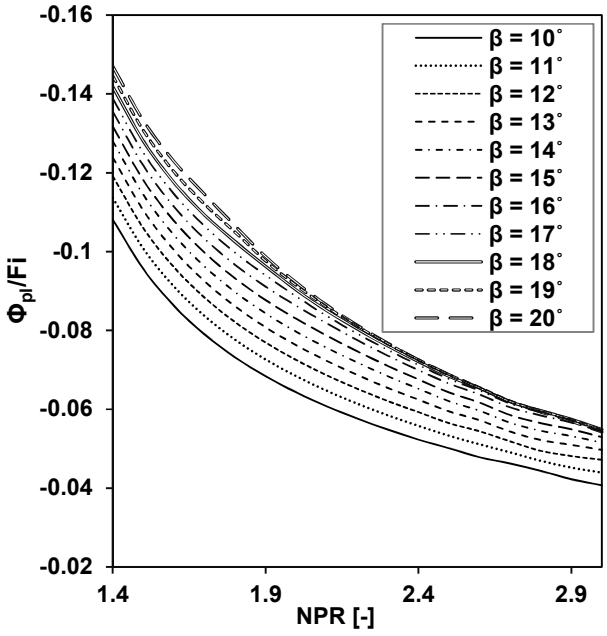


Figure 11 Pressure force of the plug (Φ_{pl}) as a function of the NPR for the chosen plug half angle (β) at operational conditions of M_∞ =0.82 and Alt =36000ft, for the configuration of CR=1.75.

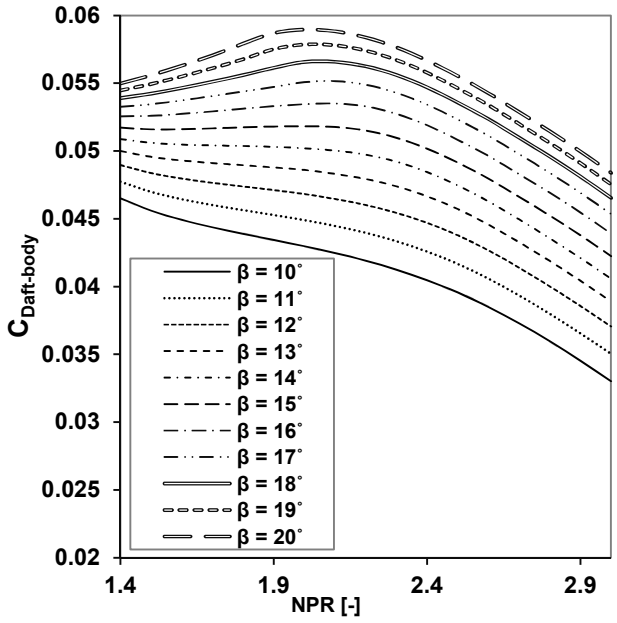


Figure 12 Pressure drag coefficient ($C_{Daft\text{-}body}$) of the cowl after-body as a function of the NPR for the chosen cone half angle (β) at operational conditions of M_∞ =0.82 and Alt =36000ft, for the configuration of CR=1.75.

3.2.3 Impact of the contraction ratio (CR)

The increase in CR has been achieved by reducing the throat area which results in a decrease in the radius of curvature of the lower aero-line (R_{c4}) of the nozzle and an increase in R_{in}, (Figure 1). This causes an increase in the

pressure over the inner wall surface with the increase in the CR. Besides that, it was found that the pressure coefficient is proportional to the NPR, (Figure 13). However, as the flow passes the nozzle hump, the behaviour of the flow shows a contrary behaviour, where the increase in the CR reduces Cp in the region between the nozzle hump and the nozzle exit plane. This is attributed to the increase in the flow velocity at the nozzle exit.

The increase in CR increases the pressure force over the plug surface, (Figure 14). The pressure force (Φ_{pl}/F_i) increased from 3.30 to 3.84 as CR was changed from 1.3 to 1.75 at NPR =3.0 and x/l_{nozzle} =0.0, (Figure 14). The combined effect of the NPR and the CR showed that at low NPR the change in Φ_{pl}/F_i is 0.0474 at NPR =1.4 between the two extreme CR levels (1.3 and 1.75) and x/l_{nozzle} =0.0, (Figure 14). This is attributed to the increase in the flow momentum flux exhausted from the nozzle with the reduction in the throat area that is associated with the increase in CR. This produced a stronger normal shock at the nozzle exit than the small CR configuration. Having different CR means the nozzle capacity and the power settings are different. Although the impact of the variation of the CR on the nozzle aerodynamics is small, it is still essential. The reason for this is the necessity to develop nozzle performance maps that apply to various engine thrust settings and capacities.

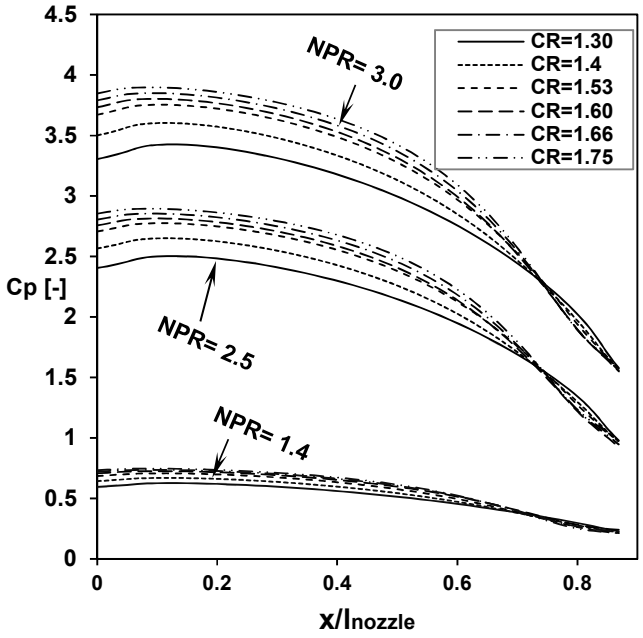


Figure 13 Pressure coefficient (Cp) distribution over the inner aero-line of the nozzle part of the bypass stream as a function of the CR for the chosen NPR for configuration of β=15˚.

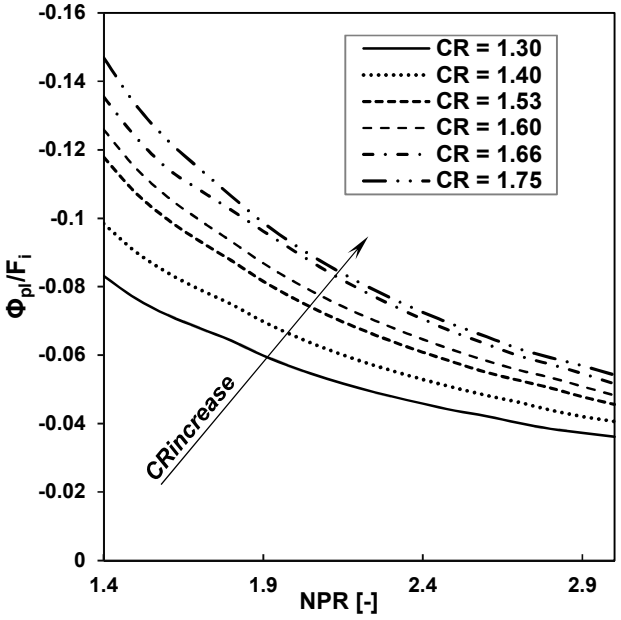


Figure 14 Plug pressure force to the ideal thrust as a function of the NPR and the CR for the chosen β at the operational condition of M_∞=0.82.

3.3 Nozzle performance maps

The nozzle maps were based on the calculation of the gross thrust coefficient ($C_{fg,}$ Equation 1). Two definitions of the nozzle gross thrust, Equations 2 and 3b, were used to calculate C_{fg1} and C_{fg2}. The maps are presented for each CR (six sets of maps) as a function of the NPR and plug half-angle (β), for the mid-cruise condition (Alt =36000ft and M_∞=0.82), (Figure 15).

The thrust coefficient profile shows a sharp growth with the variation of the NPR, across the range from 1.40 to 1.85. This is attributed to the sharp increase in the ratio of the computed to the ideal mass flow across the low range of the NPR up to the choking conditions of the nozzle. After the nozzle flow has choked, the performance in terms of C_{fg1} declines moderately. This is attributed to the decrease in the contribution of the plug pressure force to the engine thrust (see Figure 11). Moreover, across this region, the expansion losses in the nozzle flow become more noticeable.

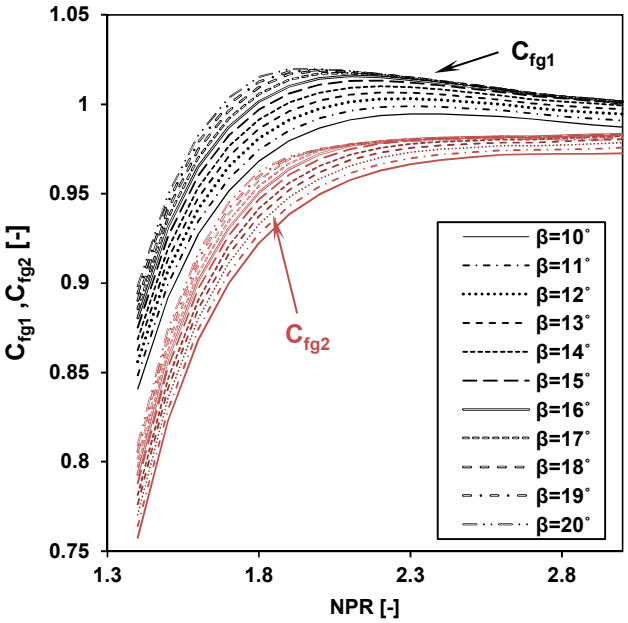
An increase in β improves the performance in terms of C_{fg1} and C_{fg2} across the range of the NPR from 1.40-1.90. However, this increase is insignificant at high levels of β (15˚ to 20˚). in which the deviation of C_{fg} due to the increase in β values starts to reduce with the NPR. For example, the reduction in C_{fg} between β =17˚ and the 18˚ is 0.02% for the configuration of CR=1.66 and NPR =3.0, whereas this difference becomes 0.14% of the same change in β and the same CR but at NPR =2.1, (Figure 15). Since

the plug pressure forces Φ_{pl}/F_iincreased with the CR, (see Figure 14), this is also reflected C_{fg1} and C_{fg2}, (Figure 15). Hence, C_{fg1} is 1.020 at NPR of 2.0 and CR =1.30, and 1.060 when CR=1.75, at NPR = 1.80. The latter is the maximum value of C_{fg} for all sets of the maps as a function of NPR and β.

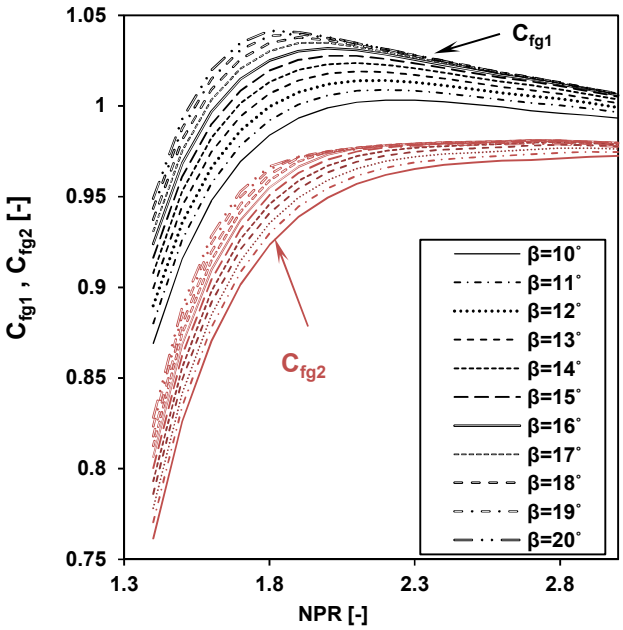
The nozzle performance in terms of C_{fg2} is significantly lower than C_{fg1}, Figure 15. The results showed that the value of C_{fg1} is higher than 1.0 at high levels of β and NPR; however, all the values of C_{fg2} are less than 1.0, (Figure 15). This indicates that the cowl after-body is contributing as a drag to the performance calculations. However, since the cowl after-body drag ($C_{Daft\text{-}body}$) reduces with the NPR and β, (Figure 12), the performance showed an improvement with the increase in NPR and β. The decrease in the drag pressure force of the cowl after-body ($C_{Daft\text{-}body}$) with the NPR caused C_{fg2} data trend to level off after the noticeable reduction in C_{fg1} data, (Figure 15). This behaviour made the difference in the performance between C_{fg1} and C_{fg2} results to reduce after NPR passes 1.90.

Overall, the performance maps provide modified and improved C_{fg} values that capture the effect of various degrees of freedom that are affecting the nozzle performance. Therefore, instead of the typical current one-dimensional maps that illustrate the NPR impact only for a single nozzle configuration[5,9,14,15,21,30], the multidimensional effect of the flow has been quantified.

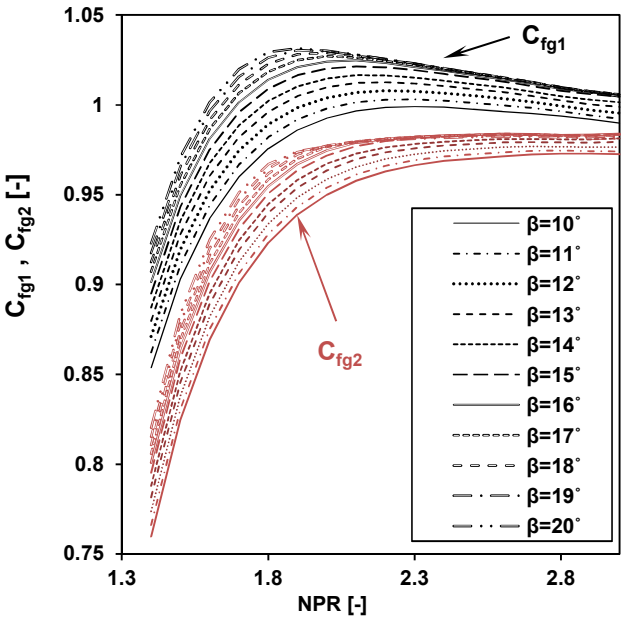
In the current work, two thrust coefficient definitions were used. One of them included the cowl after body forces in the calculation of nozzle performance. The reason behind that quantifies the impact of the external flow over the nacelle on the overall performance of the engine. Therefore, for the case when the engine is tested under static conditions, the inclusion of the cowl after-body is unnecessary.



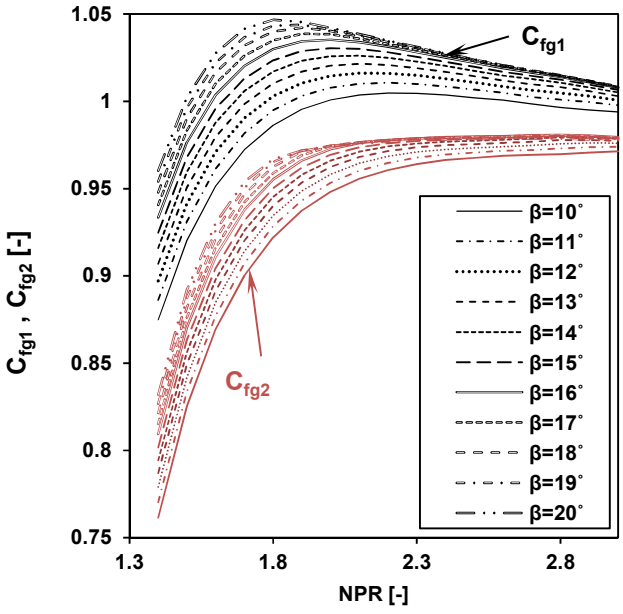
CR =1.30



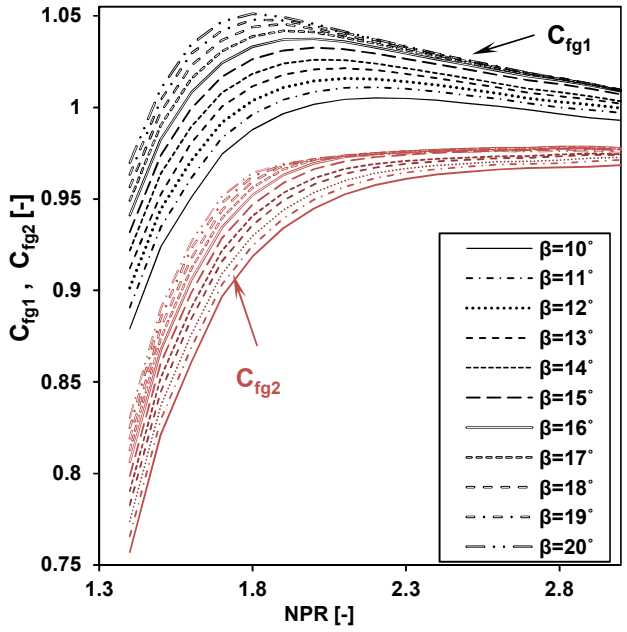
CR = 1.53



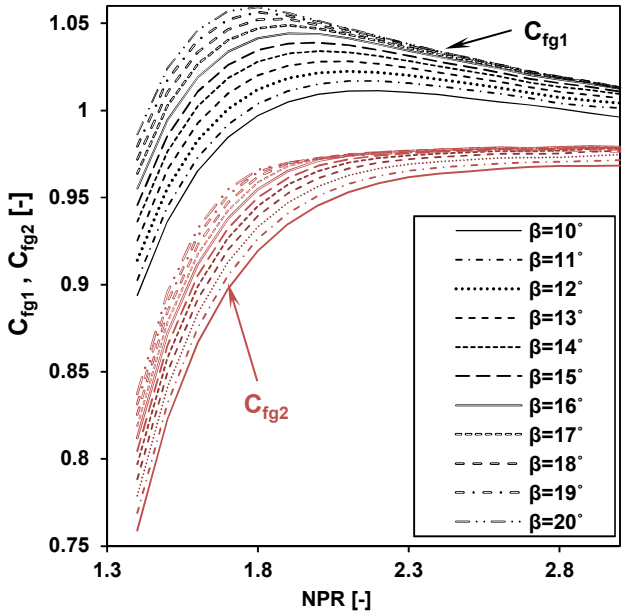
CR =1.40



CR =1.60



CR =1.66

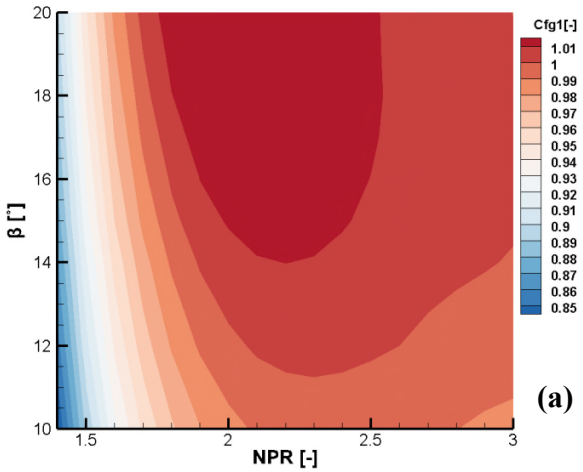


CR =1.75

Figure 15 Nozzle gross thrust coefficient maps as a function of the NPR and β for the chosen CR at mid-cruise operational conditions.

3.4 Low-order nozzle performance prediction models

The low order models were used to build the nozzle maps that have been generated based on CFD calculations, (Figure 15). For a given CR, C_{fg1} depends on NPR and β and overall the Kriging RSM model captures this dependency well in comparison with the CFD data,(Figure 16.)



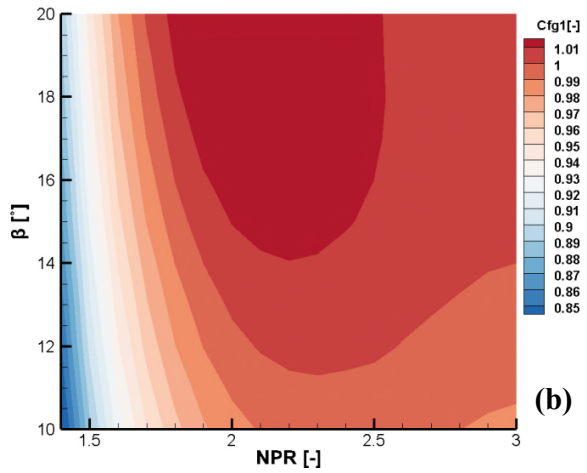
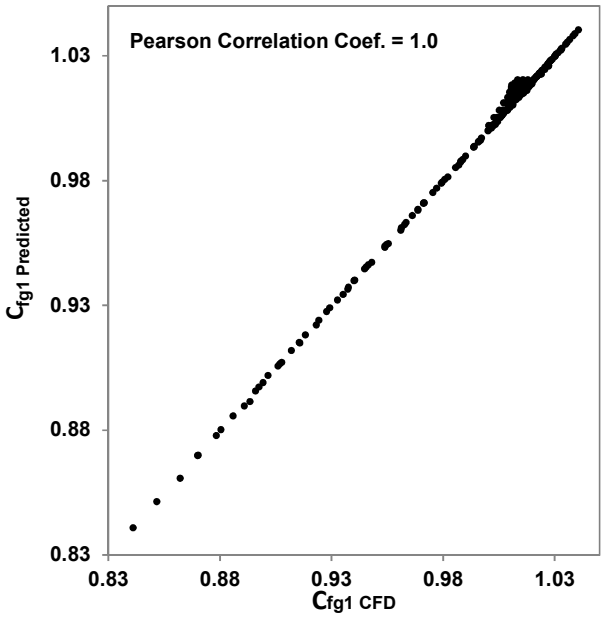
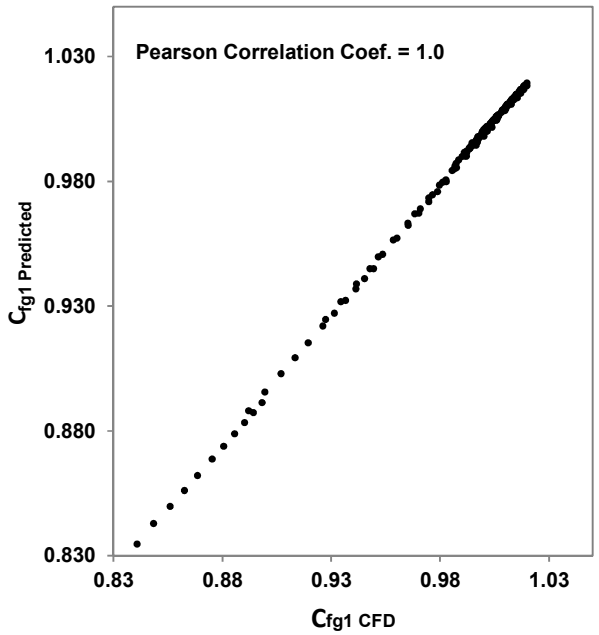


Figure 16 comparison between the CFD derived performance data and the predicted data based on the chosen low-order models for nozzle configuration of CR =1.30; (a) CFD data, (b) Kriging.

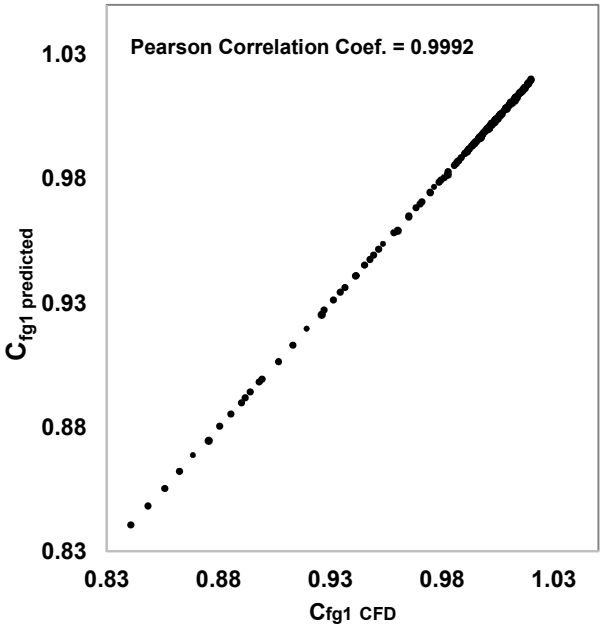
The performance of each of the employed low order models was evaluated by calculating the difference between the predicted and the CFD calculated C_{fg}. A correlation between the CFD derived data, and the low order model predicted data, was built for two degrees of freedom (NPR and β), (Figure 17). For the linear interpolation, the correlation shows a strong prediction for the CFD data across the range of low values of β and NPR. However, the data loses its fidelity at high values of β and NPR. Despite that, the Pearson correlation coefficient is 0.9995 with RMSE = 0.022, (Figure 17). For the cubic spline method, the characteristics are better captured across the full NPR range. The Pearson correlation coefficient was 1.0 with an RMSE of 0.011. The Kriging method showed a linear correlation between the predicted and CFD data with a Pearson coefficient of 0.992 and an RMSE of 0.0004.



(a)



(b)

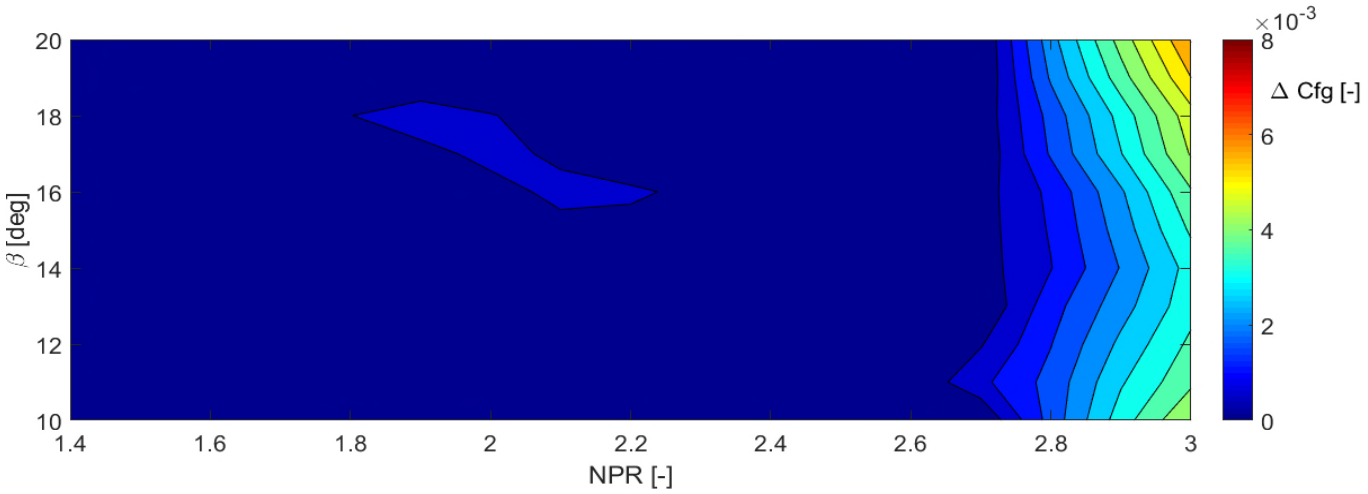


(c)

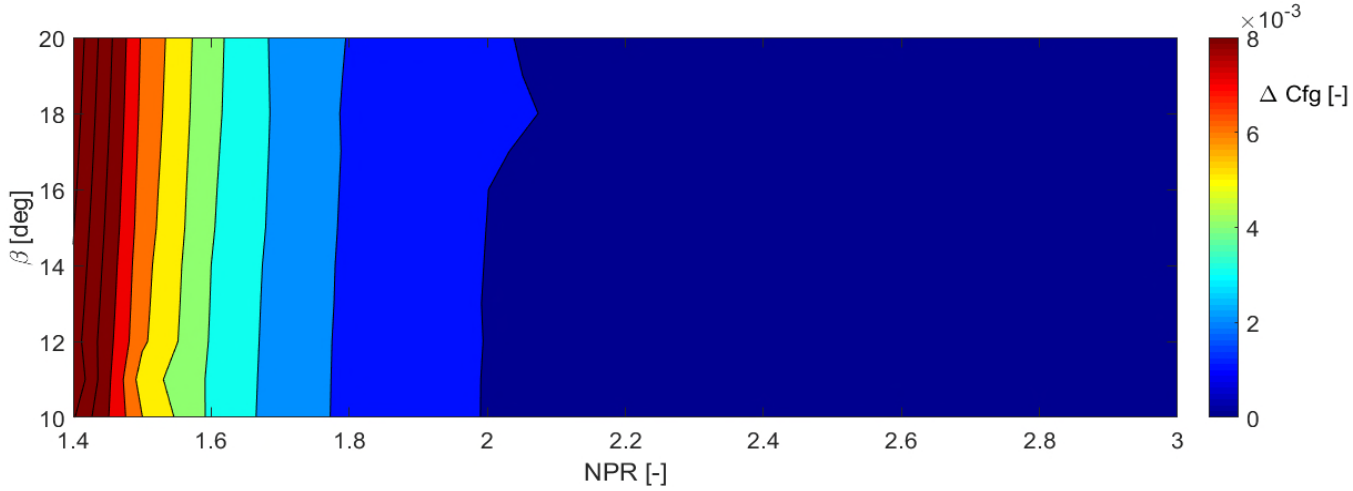
Figure 17 Correlation between the computed and the predicted gross thrust coefficient as a function of NPR and β; (a) linear, (b) cubic spline, (c) Kriging.

The discrepancy between the CFD computed, and the predicted datasets are presented in Figure 18. The linear interpolation, as a function of NPR and β, results showed that the discrepancy increased at high levels of NPR from 2.7 to 3.0. The cubic spline results showed that at a low level of NPR there is a noticeable discrepancy; however, it reduces with the increase in the NPR and β. Kriging results showed that the model predicted C_{fg1} with very close levels to the CFD one across particular ranges of NPR and β. Although the linear interpolation seems to provide the best results, however, it showed a high level of inconsistency at the high range of NRR (>2.6) due to the nonlinear behaviour of the data as a function of β. The cubic spline method showed better results and useful behaviour than the linear method across most of the NPR range. However, the local error in ΔCfg increased to approximately 0.009 at low NPR, (Figure 18 b). Kriging model is the best in the prediction of the

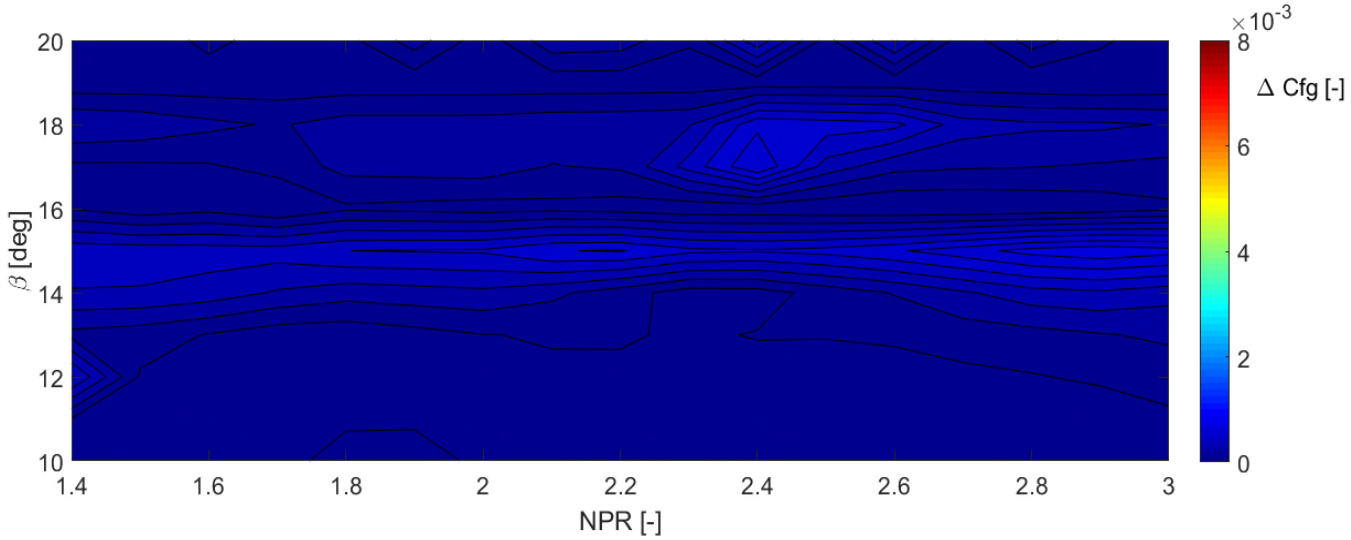
data, with very low levels of discrepancy in the order of 0.003 across the range, NPRs (Figure 18 c). These prediction models can be used to evaluate the combined impact of the aerodynamic and geometrical parameters of the nozzle over a wider range of conditions.



(a)



(b)



(c)

Figure 18 Response surface methods discrepancy for each data point of the nozzle thrust coefficient; (a) linear, (b) Cubic Spline, (c) Kriging.

4. Conclusion

This paper presents a methodology to assess the propelling nozzle performance as a function of the nozzle pressure ratio and the geometrical features. Several basic nozzle configurations were simulated using aerodynamic assessment model. Multi-dimensional maps were build based on the investigated aerodynamical and geometrical parameters. The maps are presented in terms of the nozzle gross thrust coefficient and highlight the main sensitivities of the nozzle characteristics to nozzle pressure ratio, contraction ratio and plug half-angle.

Low-order models were built on the CFD derived thrust coefficient. The low order models were validated using a leave-one-out cross-validation approach. Across the range of aerodynamic and geometric configurations, a Kriging method provided the best performance with a typical error of 0.2%.

Declaration of Conflicting Interests

The author(s) declared no potential conflicts of interest with respect to the research, authorship, and/or publication of this article.

Funding

Dr AL-Akam doctoral studies were fully funded by the Ministry of Higher Education of Iraq, which is represented by Iraqi Cultural Attaché in London.

References

1. Zucrow MJ, Hoffman JD. *Gas dynamics*. New York: Wiley, 1976.
2. Covert E. *Thrust and Drag: Its Prediction and Verification (Progress in Astronautics and Aeronautics Series)*. Cambridge: Cambridge University Press, 1985.
3. Farokhi S. *Aircraft Propulsion*. 2nd ed. Chichester, UK: Wiley, 2014.
4. Mattingly JD, Heiser WH, Pratt DT. *Aircraft Engine Design*. 2nd ed. Washington, D.C: American Institute of Aeronautics and Astronautics, 2002.
5. Thornock RL, Brown EF. An experimental study of compressible flow through convergent-conical nozzles, including a comparison with theoretical results. *J Basic Eng* 1972; 94: 926–930.
6. Zhang Y, Chen H, Zhang M, et al. Performance Prediction of Conical Nozzle Using Navier–Stokes Computation. *J Propulsion and Power* 2015; 31: 192–203.
7. Spotts NG, Guzik S, Gao X. A CFD Analysis of Compressible Flow through Convergent-Conical Nozzles. In: *49th AIAA/ASME/SAE/ASEE Joint Propulsion Conference*. CA: American Institute of Aeronautics and Astronautics, AIAA 2013-3734, 2013.
8. Dippold VF. *Computational simulations of convergent nozzles*. Technical Report, Technical Report, NASA Glenn Research Center, NASA/TM-2014-218329; E-18926; GRC-E-DAA-TN14457, 2014.

9. Lennard DJ and WAF. Performance Improvement Features of General Electric Turbofan Engines, ASME 82-GT-270. In: *The American Socity of Mechanical Engineers*. New York: ASME 82-GT-270, 1982.

10. Lahti DJ, Dietrich DA, Stockman NO, et al. Application of Computational Methods to the Design of Large Turbofan Engine Nacelles. In: *AlAA 22nd Aerospace Sciences Meeting*. Reno, Nevada: AlAA 84-0121, 1984, pp. 1–12.

11. Malecki R, Lord W. A 2D Duct / Nozzle Navier-Stokes Analysis System for Use By Designers. In: *31st AIAA/ASME/SAE/ASEE Joint Propulsion Conference and Exhibit*. San Diego, CA: AIAA 95-2624, 1995, pp. 1–19.

12. Zimmermann H, Gumucio R, Katheder K, et al. CFD Study of Nozzle Configurations for Ultra High Bypass Engines. In: *International Gas Turbine and Aeroengine Congress and Exposition*. Cincinnati, Ohio: ASME93-GT-389, 1993, pp. 1–14.

13. Zimmermann H, Katheder K and, Jula A. A numerical investigation into the nozzle flow of high by-pass turbofans. In: *International Gas Turbine and Aeroengine Congress and Exposition*. Cologne, Germany: ASME 92-GT-10, 1992, pp. 1–11.

14. Malecki R, Lord W. Aerodynamic performance of exhaust nozzles derived from CFD simulation. In: *31st AIAA/ASME/SAE/ASEE Joint Propulsion Conference and Exhibit*. San Diego, CA: AIAA 95-2623, 1995, pp. 1–17.

15. Mikkelsen KL, Myren DJ, Dahl DG, et al. Initial Subscale Performance Measurements of the AIAA Dual Separate Flow Reference (DSFR) Nozzle. In: *51st AIAA/SAE/ASEE Joint Propulsion Conference*. Orlando,USA: AIAA 2015-3883, 2015, pp. 1–30.

16. Kulfan B, Bussoletti J. ‘Fundamental’

parametric geometry representations for aircraft component shapes. In: *11th AIAA/ISSMO Multidisciplinary Analysis and Optimization Conference*. Seattle, Washington: AIAA-2006-6948, 2006, pp. 547–591.

17. Williams D. Propulsion system performance and integration. *Lecture note, Cranfield University*.
18. MacMillan WL. *Development of a modular-type computer program for the calculation of gas turbine off-design performance*. PhD Thesis, Cranfield University,UK, 1974.
19. Roache PJ. *Verification and Validation in Computational Science and Engineering*. Hermosa: Hermosapublishers, 2014.
20. ANSYS Inc. ANSYS Fluent Theory Guide 14.0, November,2013.
21. Harrington DE. *Performance of Convergent and Plug Nozzles at Mach Numbers from 0 to 1.97*. NASA Technical Memorandum-NASA TM X-2112, 1970.
22. Goulos I, Stankowski T, Otter J, et al. Aerodynamic Design of Separate-Jet Exhausts for Future Civil Aero-engines—Part I: Parametric Geometry Definition and Computational Fluid Dynamics Approach. *J Eng Gas Turbines Power* 2016; 138: 81201–81214.
23. Venter G, Haftka R, Chirehdast M, et al. Response surface approximations for fatigue life prediction. In: *38th Structures, Structural Dynamics, and Materials Conference*. Florida, U.S.A.: AIAA-97-1331, 1997.
24. Box GEP, Draper NR. *Empirical Model-building and Response Surface*. New York, NY, USA: John Wiley & Sons, Inc., 1986.
25. Press WH, Teukolsky SA, Vetterling WT, et al. *Numerical Recipes in FORTRAN; The Art of Scientific Computing*. 2nd ed. New York, NY, USA: Cambridge University Press, 1993.

26. Forrester AIJ, Sobester A, Keane AJ. *Engineering Design via Surrogate Modelling: A Practical Guide*. Chichester, UK: Wiley and Sons, 2008.

27. Casella G, Fienberg S, Olkin I. *An Introduction to statistical learning*. Seventh Ed. New York Heidelberg Dordrecht London: Springer, 2013.

28. Chapra SC, Canale RP. *Numerical Methods for Engineers: With Programming and Software Applications*. 3rd ed. New York, NY, USA: McGraw-Hill, Inc., 1997.

29. Palmer G. Construction of CFD Solutions Using Interpolation Rather than Computation with the ADSI Code. In: *47th AIAA Aerospace Sciences Meeting including The New Horizons Forum and Aerospace Exposition*. Orlando,USA: AIAA 2009-141, 2009.

30. Mattingly JD, Ohain H Von. *Elements of propulsion : Gas turbines and rockets*. Virginia, USA: American Institute of Aeronautics and Astronautics, Inc, 2006.

Appendix

Notation

A	*area, [m2]*
$Alt.$	*altitude, [m]*
C_d	*discharge coefficient*
C_{fg}	*gross thrust coefficient*
CFD	*computational fluid dynamics*
CFL	*Courant Friedrichs Lewy number*
Cp	*pressure coefficient* $= \frac{p-p_\infty}{0.5\rho U_\infty^2}$
CR	*contraction ratio*
CST	*Class-Shape-Transformation*
CV	*Cross-validation*
D	*diameter, [m]*
F_G	*gross thrust, [kN]*
f	*Physical property of interest*
GCI	*grid convergence index*
H	*CFD domain height, [m]*
l	*length, [m]*
$\dot{m}$	*mass flow rate, [kg/s]*
M	*Mach number*
NPR	*nozzle pressure ratio*
p	*static pressure, [pa]*
P	*Total pressure, [pa]*
R	*radius, [m]*
R_{ci}	*Radius of curvature at the specified location, [m]*
T	*temperature, [K]*
U	*velocity, [m/s]*
W	*CFD domain width, [m]*
α	*Nozzle curves angle, [°]*
β	*Plug half-angle, [°]*
θ	*Momentum thickness, [m]*
γ	*heat capacity ratio*
ρ	*density, [kg/m3]*
τ	*Wall shear stress, [pa]*

Subscripts

a	*actual*
Aft-body	*After-body*
c	*curvature*
bt	*Boat tail*
CP	*charging plane*
Crit.	*critical*
th	*throat*
i	*ideal*
in	*inner*
max	*maximum*
mini	*minimum*
o	*outer*
pl	*plug*
ref	*Reference*
s	*Isentropic*
t	*Total*
∞	*free stream conditions*



https://dspace.org/

Computational fluid dynamics-based approach for low-order models of propelling nozzle performance

Al-Akam, Aws A.; Nikolaidis, Theoklis; MacManus, David G.

2019-03-14
Institution of Mechanical Engineers
https://doi.org/10.1177/0954410019831852
Al-Akam A, Nikolaidis T, MacManus DG. (2019) Computational fluid dynamics-based approach for low-order models of propelling nozzle performance. Proceedings of the Institution of Mechanical Engineers, Part G: Journal of Aerospace Engineering, Volume 233, Issue 13, October 2019, pp. 4879-4894

Downloaded from a DSpace repository. https://dspace.org/